INTERNATIONAL JOURNAL FOR NUMERICAL METHODS IN ENGINEERING
Int. J. Numer. Meth. Engng 2003; **56**:1647–1659 (DOI: 10.1002/nme.632)

Plotting holographic interferograms for visualization of dynamic results from finite-element calculations

M. Ragulskis[1,*,†], A. Palevicius[1] and L. Ragulskis[2]

[1]*Faculty of Informatics, Kaunas University of Technology, Kaunas, Lithuania*
[2]*Faculty of Informatics, Vytautas Magnus University, Kaunas, Lithuania*

SUMMARY

Procedures for plotting computer generated interferograms from the results of finite-element analysis based on the principles of optical holography can provide a realistic view of dynamic processes taking place in the analysed structures. Such visualization is based on a solid physical background, does not require animation for representing dynamic processes, and is also important from the point of view of interpretation of experimental holograms.

The numerical method for obtaining time-averaged digital interferograms for structural dynamics applications is presented. Intensity mapping as well as the methods of digital stroboscopic analysis are used for plotting clearer images due to the fact that the intensity of higher interference bands decreases rapidly with the growth of vibration amplitudes.

The digital time averaging of intermediate states of the moving surface together with varying direction of incident laser beam and estimation of diffuse and specular reflection phenomena enables the generation of realistic interferograms. Such a procedure is scalable in parallel computations and applicable to a wide variety of problems. Copyright © 2003 John Wiley & Sons, Ltd.

KEY WORDS: holographic interferometry; finite-element method; digital interferogram

INTRODUCTION

The amount of data produced by finite-element calculation places a particular challenge to scientific visualization. Meaningful and accurate visualization is an important task of computer modelling [1]. That is especially significant for structural dynamics applications.

Structural dynamics finite-element method (FEM) results can be presented as a set of slides each corresponding to static deformations at appropriate time moments (plots, graphs or animations), or a skeleton grid map representing two or more positions of maximum displacements. Such methods of visualization usually give clear representation of dynamic processes taking place in the analysed structure, but they have several drawbacks.

*Correspondence to: M. Ragulskis, P.O. Box 1300, LT-3028, Kaunas, Lithuania
†E-mail: minvydas.ragulskis@fmf.ktu.lt

Received 7 June 2001
Revised 1 March 2002
Accepted 24 April 2002

The first is related to the conceptual principle of linear FEM theory [2, 3] which is based on the proposition that all displacements are small (that is not true for large displacement FEM theory). The exaggeration of nodal displacements relatively to the geometrical dimensions of the analysed structure has no physical background.

Another drawback takes place when complicated structures consisting of several interacting bodies are analysed. The exaggerated displacements can give good basic knowledge about dynamics of separate subsystems but impair the general view of the whole system's dynamics. Example could be models of ultrasonic motors, when vibrating piezo-ceramic elements bring the output element into translatory (or rotary) motion. It would be quite difficult to couple pictures of the operating elements together if the dynamic deflection shapes would be constructed using exaggerated displacements.

Visualization of structural displacements from FEM results is a common procedure. Many commercial packages have facilities for performing such visualization in the form of three-dimensional (3D) maps, colour or isoline plots, animation pictures, etc. More advanced graphical procedures utilize spline, fringe contours plotting technology [4, 5].

Different optical methods are used for the visualization of vibrating structures. One of the most effective techniques for physical visualization of structural micro-vibrations is the method of holographic interferometry [6–9]. This enables one to assume that dynamic FEM results can be presented in a form of interferograms providing more accurate physical interpretation of the structural vibrations.

Procedures plotting computer generated interferograms from the results of FEM analysis based on the principles of optical holography can provide realistic view of dynamic processes taking place in the analysed structures. Such visualization is based on solid physical background, does not require animation for representing dynamic processes, and is also important from the point of view of interpretation of experimental holograms.

Although the interpretation of fringes of the generated interferograms is not straightforward and requires some knowledge about the physical principles of holography, it can be successfully exploited in the process of analysis of optical holograms. The full hybrid approach of experimental–numerical concept of analysis is presented in Reference [10]. The numerical model is iteratively modified in order to achieve full agreement between experimental and numerical data. So a set of experimentally based finite-element models can be used for plotting holographic interferograms and comparisons with the experimental ones.

THEORETICAL BACKGROUND

The basic principle of the formation of interference bands can be illustrated by an example of a vibrating bar (Figure 1). If harmonic vibration of the bar is defined as

$$Z(x)\sin\omega t \tag{1}$$

then the characteristic function defining the complex amplitude of the laser beam M_T in the plane of the hologram takes the form [6]:

$$M_T = \lim_{T\to\infty} \frac{1}{T}\int_0^{\mathrm{T}} \exp\left(\mathrm{i}\left(\frac{4\pi}{\lambda}\right) Z(x)\sin\omega t\right)\mathrm{d}t = J_0\left(\left(\frac{4\pi}{\lambda}\right) Z(x)\right) \tag{2}$$

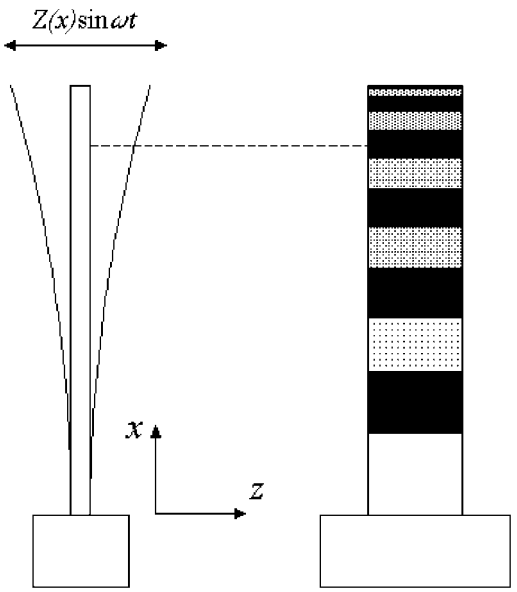

Figure 1. The principle of formation of interference bands.

where T is the exposure time of the hologram, $(T \gg 1/\omega)$; ω is the frequency of structural vibrations, λ is the laser wavelength; and J_0 is the zero order Bessel function of the first type. Then, the resulting intensity I of the point (x, y) on the hologram is

$$I(x, y) = a^2(x, y)|M_T|^2 \tag{3}$$

where $a(x, y)$ is the distribution of the amplitude of the incident laser beam.

It can be noted that the centres of dark interference bands in the holographic interferogram coincide with such values of $Z(x)$ which turn the Bessel function to zero. The structure of the distribution of the interference bands does not depend on the static deformations of the structure, nor from the distance between the structure and the hologram.

THE COUPLING OF THE FEM MODEL WITH OPTICAL RELATIONSHIPS

Let the planes A and B be defined in the three-dimensional space (Figure 2). Let the triangle defined by points 1, 2 and 3 be located in the plane A. This triangle is interpreted as an elementary body surface unit meshed using the FEM. Let the co-ordinates of the point r_1 define the observation point and the projection plane be defined by the points r_2, r_3 and r_4:

$$r_i = (x_i, y_i, z_i), \quad i = 1, 2, 3, 4 \tag{4}$$

where r_2 is the origin of the projection plane and the vectors $(r_3 - r_2)$, $(r_4 - r_2)$ form the ortho-normal base of the projection plane. The L-co-ordinates of the point of intersection of the line defined by the point of the structure (x, y, z) and the observation point with the

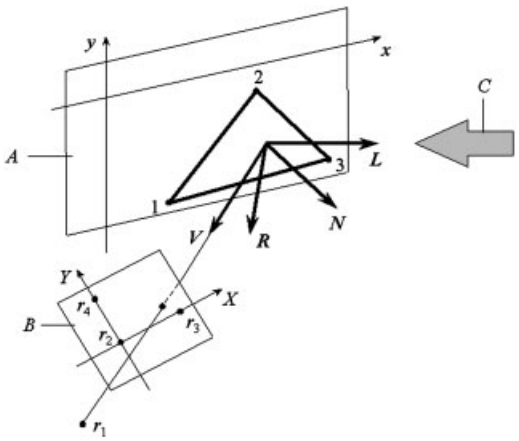

Figure 2. Determination of the intensity of the surface: A—plane of the structure, B—projection plane, C—the incident laser beam.

projection plane can be obtained using the relationship in Appendix A, where the system matrix is substituted by

$$\begin{bmatrix} x_2 & x_3 & x_4 & -x_1 & -x \\ y_2 & y_3 & y_4 & -y_1 & -y \\ z_2 & z_3 & z_4 & -z_1 & -z \\ 1 & 1 & 1 & 0 & 0 \\ 0 & 0 & 0 & 1 & 1 \end{bmatrix} \tag{5}$$

Then the spatial co-ordinates of the point of intersection $(\tilde{x}, \tilde{y}, \tilde{z})$ are:

$$\begin{aligned} \tilde{x} &= L_4 x_1 + L_5 x \\ \tilde{y} &= L_4 y_1 + L_5 y \\ \tilde{z} &= L_4 z_1 + L_5 z \end{aligned} \tag{6}$$

The co-ordinates of the point (X, Y) in the projection plane can be obtained:

$$\begin{aligned} X &= (\tilde{x} - x_2)(x_3 - x_2) + (\tilde{y} - y_2)(y_3 - y_2) + (\tilde{z} - z_2)(z_3 - z_2) \\ Y &= (\tilde{x} - x_2)(x_4 - x_2) + (\tilde{y} - y_2)(y_4 - y_2) + (\tilde{z} - z_2)(z_4 - z_2) \end{aligned} \tag{7}$$

Assuming the projection plane corresponds to the computer graphical screen and contains n rows and m columns of pixels, the calculations are performed for every pixel of the mapped

interferogram:

$$\begin{aligned} X &= X_{\min} + (j-1)(X_{\max} - X_{\min})/(m-1) \\ Y &= Y_{\max} - (i-1)(Y_{\max} - Y_{\min})/(n-1) \\ i &= 1,\ldots,n;\ j=1,\ldots,m \end{aligned} \tag{8}$$

where the subscripts min and max indicate the minimum and maximum values of the corresponding quantities.

The unit normal vector of the projection plane is

$$\begin{aligned} x_0 &= (y_3 - y_2)(z_4 - z_2) - (z_3 - z_2)(y_4 - y_2) \\ y_0 &= (z_3 - z_2)(x_4 - x_2) - (x_3 - x_2)(z_4 - z_2) \\ z_0 &= (x_3 - x_2)(y_4 - y_2) - (y_3 - y_2)(x_4 - x_2) \end{aligned} \tag{9}$$

Finally the spatial co-ordinates (x^*, y^*, z^*) of the point in the projection plane can be determined from

$$\begin{bmatrix} x_3 - x_2 & y_3 - y_2 & z_3 - z_2 \\ x_4 - x_2 & y_4 - y_2 & z_4 - z_2 \\ x_0 & y_0 & z_0 \end{bmatrix} \begin{Bmatrix} x^* \\ y^* \\ z^* \end{Bmatrix} = \begin{Bmatrix} X + x_2(x_3 - x_2) + y_2(y_3 - y_2) + z_2(z_3 - z_2) \\ Y + x_2(x_4 - x_2) + y_2(y_4 - y_2) + z_2(z_4 - z_2) \\ x_2 x_0 + y_2 y_0 + z_2 z_0 \end{Bmatrix} \tag{10}$$

It is assumed that the analysed structure is located in the plane $z = 0$ in the status of equilibrium, and $(\hat{x}_i, \hat{y}_i)$, $i = 1, 2, 3$ are nodal co-ordinates of a linear triangle element. Then the L-co-ordinates can be determined using the relationship in Appendix A, where the system matrix is substituted by

$$\begin{bmatrix} \hat{x}_1 & \hat{x}_2 & \hat{x}_3 & -x_1 & -x^* \\ \hat{y}_1 & \hat{y}_2 & \hat{y}_3 & -y_1 & -y^* \\ 0 & 0 & 0 & -z_1 & -z^* \\ 1 & 1 & 1 & 0 & 0 \\ 0 & 0 & 0 & 1 & 1 \end{bmatrix} \tag{11}$$

Thus, the approximate co-ordinates of the intersection point $(\alpha, \beta, 0)$ between the line through the observation point and the pixel (i, j) and the surface of the analysed structure are obtained by interpolation.

It is assumed that the laser rays are coherent and parallel to each other.

The unit vector L from the point of the structure in the state of equilibrium to the isophase cross-section of the laser beam in the direction of the beam is predefined.

The normal vector N coincides with the unit vector of the z-axis:

$$N = [N_x, N_y, N_z]^{\mathrm{T}} = [0, 0, 1]^{\mathrm{T}} \tag{12}$$

The relationship between the direction to the light source and the direction of reflection can be described by the following equation [11]:

$$R = \begin{bmatrix} 2N_x^2 - 1 & 2N_xN_y & 2N_xN_z \\ 2N_xN_y & 2N_y^2 - 1 & 2N_yN_z \\ 2N_xN_z & 2N_yN_z & 2N_z^2 - 1 \end{bmatrix} L \tag{13}$$

where R is the direction of reflection. The vectors L, N, R (Figure 2) are complanar, the angle between L and N is equal to the angle between N and R.

Higher-order elements can be subdivided into triangles and the approximate local co-ordinates of the element can be obtained by interpolation from the local co-ordinates of the nodes of the triangle.

For the three-dimensional problem the calculations are performed for a sequential number of values of the local co-ordinates (ξ, η) in the current finite element:

$$\begin{aligned} \xi &= -1 + \frac{2}{n-1}(i-1), \quad i = 1, \ldots, n \\ \eta &= -1 + \frac{2}{n-1}(j-1), \quad j = 1, \ldots, n \end{aligned} \tag{14}$$

The spatial orthogonal Cartesian co-ordinates of these points can be calculated using the shape functions of the analysed finite element. Afterwards the corresponding values X and Y are obtained from Equation (7).

The reconstructed digital image consists of the matrix of pixels where the columns are indexed from 0 to m_x and the rows—from 0 to m_y. Thus the point (X, Y) is mapped to the pixel (i_x, i_y):

$$\begin{aligned} i_x &= \text{round}\left(\frac{X - X_{\min}}{X_{\max} - X_{\min}} m_x\right) \\ i_y &= \text{round}\left(m_y - \frac{Y - Y_{\min}}{Y_{\max} - Y_{\min}} m_y\right) \end{aligned} \tag{15}$$

The rounding operation in Equation (15) can distort the quality of the reconstructed image, especially when the resolution of the digital image is low, or the density of interference bands is high. Therefore, the shift operation to the co-ordinates of the centre of the corresponding pixel (i_x, i_y) is introduced:

$$\begin{aligned} X &= i_x \frac{X_{\max} - X_{\min}}{m_x} + X_{\min} \\ Y &= Y_{\min} - (i_y - m_y) \frac{Y_{\max} - Y_{\min}}{m_y} \end{aligned} \tag{16}$$

Now, the spatial co-ordinates of the centre of the pixel (x^*, y^*, z^*) can be calculated from Equation (10). As the projection of the analysed point on the surface of the structure does not necessary coincide with the centre of the pixel, the further calculations are dedicated for the location of a point on the surface corresponding to the centre of that pixel.

The tangential vectors to the surface of the analysed finite element

$$\begin{bmatrix} x_\xi & y_\xi & z_\xi \\ x_\eta & y_\eta & z_\eta \end{bmatrix} \tag{17}$$

are determined by multiplying the derivatives of the shape functions (with respect to the local co-ordinates) by the nodal co-ordinates of the corresponding finite element. Subscripts in Equation (17) denote partial derivatives.

The L-co-ordinates of intersection of the line (guided through the observation point and the centre of the pixel) with the plane tangential to the analysed finite element are obtained from the relationship in Appendix A, where the system matrix is substituted by

$$\begin{bmatrix} x & x+x_\xi & x+x_\eta & -x_1 & -x^* \\ y & y+y_\xi & y+y_\eta & -y_1 & -y^* \\ z & z+z_\xi & z+z_\eta & -z_1 & -z^* \\ 1 & 1 & 1 & 0 & 0 \\ 0 & 0 & 0 & 1 & 1 \end{bmatrix} \tag{18}$$

Thus the calculations are performed for the corrected local co-ordinates $(\xi + L_2, \eta + L_3)$. It can be noted that such modifications make the procedure more precise and lower the noise effects in the reconstructed interferograms.

The normal vector N for the analysed three-dimensional structure is obtained as a normalized vector product of the rows of (17). Other relationships used in the process of calculations coincide with the previously described ones for planar structures.

DETERMINATION OF THE INTERFERENCE BANDS

The distribution of intensity of the laser beam $a^2(x, y)$ is assumed [6]:

$$a^2(x, y) = I_L(k_d(NL) + k_s(VR)^n) \tag{19}$$

where I_L is the intensity of the incident laser beam, k_d is the diffuse reflection coefficient, k_s is the specular reflection coefficient, n is a coefficient describing the smoothness of the surface, V is the direction to the viewer.

When the surface of the plate performs harmonic oscillations according to an appropriate eigenform, the intensity can be calculated on the basis of Equation (3):

$$I = (\overline{\cos(4\pi(uL)\sin\omega t/\lambda)})^2 a^2(x, y) \tag{20}$$

where u is the amplitude of harmonic oscillations, λ is the laser wavelength, the top line denotes averaging by time.

The first term of Equation (20) corresponds to the direct calculation of the real part of Equation (2); the imaginary part is infinitesimal:

$$\lim_{T\to\infty} \frac{1}{T} \int_0^T \sin\left(\frac{4\pi}{\lambda}(uL)\sin\omega t\right) \mathrm{d}t = 0 \tag{21}$$

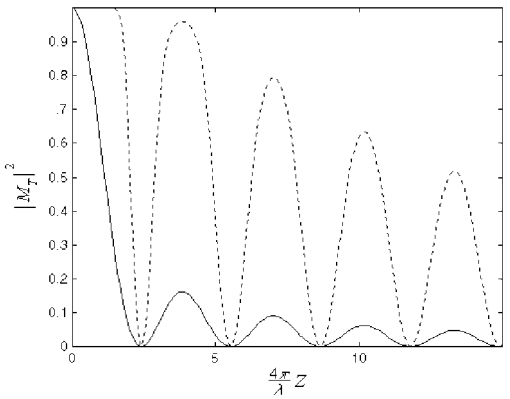

Figure 3. The decay of intensity for the time-averaged method without (solid line) and with intensity mapping at $k=5$ (dashed line).

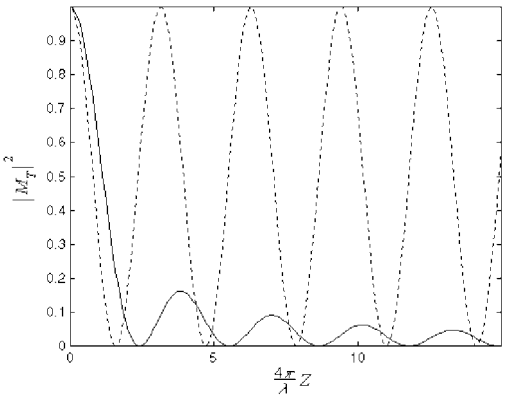

Figure 4. The decay of intensity for the time-averaged method (solid line) and for the stroboscopic method (dashed line).

Numerical averaging of Equation (20) can be performed using a certain number of intermediate state positions of the surface during one cycle of oscillations. The averaged term takes the form

$$\overline{\cos(4\pi(uL)\sin\omega t/\lambda)} = \frac{1}{n}\sum_{i=1}^{n}\cos\left(\frac{4\pi}{\lambda}(uL)\sin\frac{2\pi(i-1)}{n}\right) \tag{22}$$

It can be noted that such averaging procedure enables the generalization of the calculation of intensity for more complex (not only harmonic) dynamic processes. The convergence of the square of Equation (22) to the square of Equation (2) can be analysed numerically. It can be noted that when $n=16$ the precision of calculations is acceptable for the first three interference bands, when $n=32$—for the first five bands, when $n=64$—for the first eight bands.

The intensity levels decrease rapidly with the number of the intereference band due to the qualities of Bessel functions. As a limited number of intensity levels is used for the digital representation of images for better visualization of the results of calculations a sigmoidal mapping function is used to distort the intensity scale:

$$F(I) = \frac{\tanh(kI)}{\tanh(k)} \tag{23}$$

where parameter k characterizes the level of distortion, $0<k<\infty$ (Figure 3). It can be noted, that

$$\begin{aligned} F(0) &= 0 \\ F(1) &= 1 \\ \lim_{k\to\infty} F(I) &= \operatorname{sign}(I) \\ \lim_{k\to 0} F(I) &= I \end{aligned} \tag{24}$$

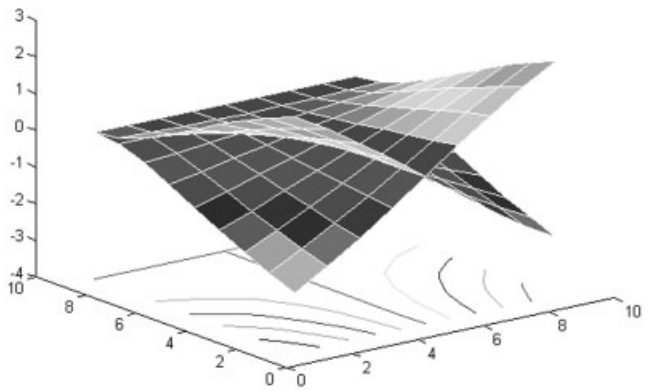

Figure 5. Extreme displacements of the second eigenmode of the plate.

In fact,

$$\lim_{k\to 0}\frac{\mathrm{d}F(I)}{\mathrm{d}I}=\lim_{k\to 0}\frac{\mathrm{e}^{k}+\mathrm{e}^{-k}}{\mathrm{e}^{k}-\mathrm{e}^{-k}}\frac{\mathrm{d}}{\mathrm{d}I}\left(\frac{\mathrm{e}^{kI}-\mathrm{e}^{-kI}}{\mathrm{e}^{kI}+\mathrm{e}^{-kI}}\right)=\lim_{k\to 0}\frac{2k}{\mathrm{e}^{k}-\mathrm{e}^{-k}}=1 \tag{25}$$

Optical stroboscopic method is used for better interpretation of micro-vibrations [6]. The structure is lightened 2 times per period of oscillations at the moments of extreme deflections.

The term $\overline{\cos(4\pi(uL)\sin\omega t/\lambda)}$ is interpreted as the average value of the two extreme deflections of the structure, corresponding to the moments $\omega t=\pi/2$ and $\omega t=3\pi/2$, so the averaged term takes the form $\cos(4\pi(uL)/\lambda)$ due to the evenness of the cosine function. Equation (20) is transformed to

$$I=\cos^{2}(4\pi(uL)/\lambda)I_{\mathrm{L}}(k_{\mathrm{d}}(NL)+k_{\mathrm{s}}(VR)^{n}) \tag{26}$$

The decay of intensities for the time averaged and stroboscopic models are presented in Figure 4. It can be noted that the locations of the centres of dark interference bands for the stroboscopic method (dashed line) do not coincide with the time-averaged ones (solid line).

The stroboscopic method does not produce a fast decay of the intensities and thus enables the interpretation of the higher interference bands from the interferogram. Thus, the visualization of higher amplitudes (higher interference bands) requires either the intensity mapping of the time-averaged interferograms, or application of the stroboscopic method of analysis.

NUMERICAL EXPERIMENT

The bending of a rectangular plate with a motionlessly clamped edge is analysed. The finite-element model with the independent approximations of the displacement and the rotations is used [3] and the first eigenmodes are calculated. The extreme displacements of the second eigenmode are shown in Figure 5. The digital holographic images of eigenvibrations are obtained using the previously described method of construction of the holographic interference bands (Figure 6). It is evident that with the increase of the amplitude of vibrations, the sharpness of the image decreases.

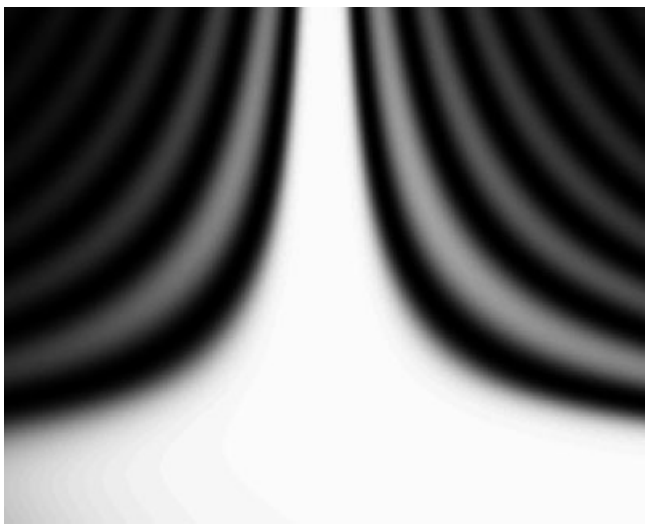

Figure 6. The time-average holographic interferogram of the second eigenmode.

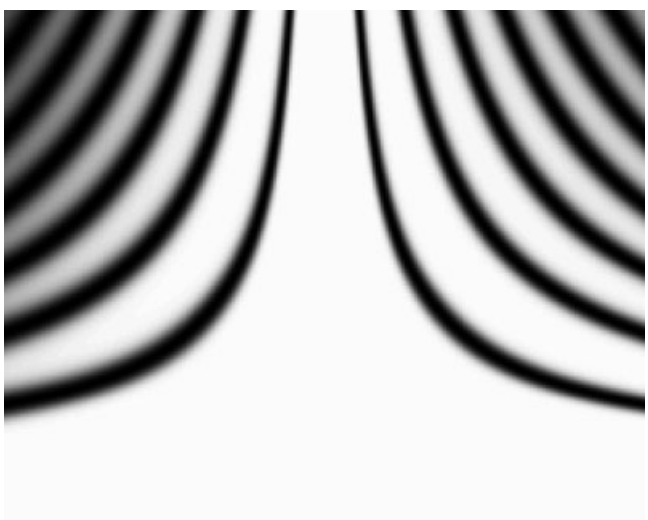

Figure 7. The time-averaged holographic interferogram of the second eigenmode with intensity mapping.

The same image with the distorted representation of intensities is shown in Figure 7.

The stroboscopic method produces an image of better sharpness (Figure 8), moreover the method requires a smaller amount of calculations.

It should be noted that in all presented interferograms the laser beam is not perpendicular to the surface of the analysed plate in the state of equilibrium. The generation of the holographic

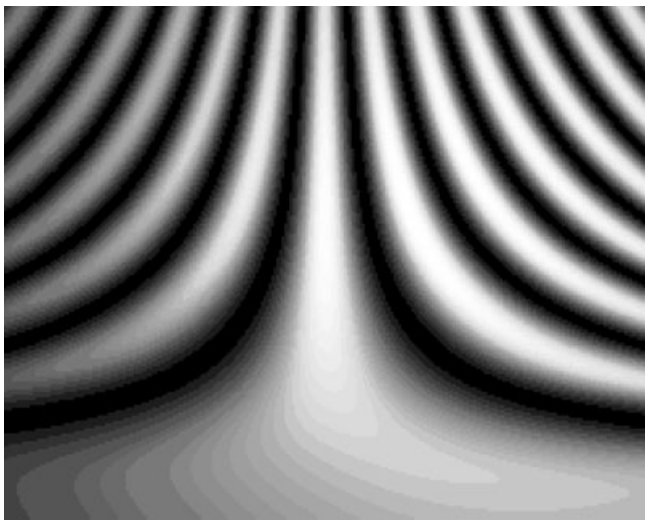

Figure 8. The stroboscopic holographic interferogram of the second eigenmode.

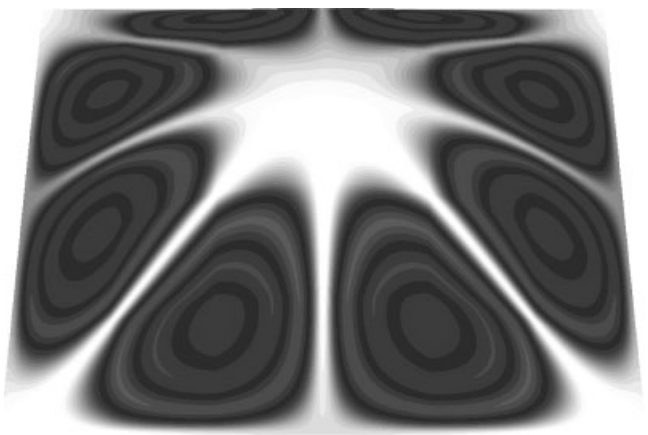

Figure 9. The time-averaged holographic interferogram of the ninth eigenmode of the shell type structure.

interferograms with various directions of the incident beam enables better interpretation of the vibrations of the structure as indicated in Reference [6].

The application of the described methodology for the formation of interferograms for shell type structures is illustrated by the digital holographic images of a shell with fixed boundaries. The generated holograms in Figures 9 and 10 present the ninth eigenmode of the shell type structure.

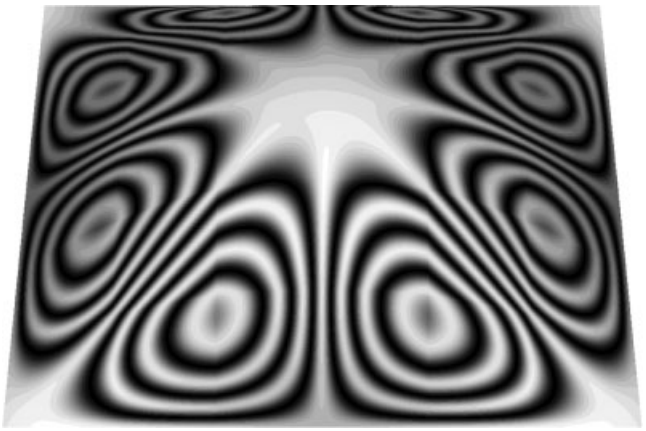

Figure 10. The stroboscopic holographic interferogram of the ninth eigenmode of the shell type structure.

CONCLUSIONS

The problem of visualization of micro-vibrations is important in engineering of precise mechanical systems. The plotting of interference bands from the results of finite-element analysis has clear physical background compared to other visualization techniques. Also that is important because of the ability of direct comparisons with the experimental results of holographic optical analysis. The presented methodology for plotting holographic interferograms is scalable in parallel computations and applicable to a wide variety of problems.

APPENDIX A

Denoting shape functions L_1, L_2 and L_3 as L-co-ordinates of the triangle [2], and L_4 and L_5 as L-co-ordinates of the line, the following relationships are true:

$$\begin{aligned} x &= L_1 x_1 + L_2 x_2 + L_3 x_3 \\ y &= L_1 y_1 + L_2 y_2 + L_3 y_3 \\ z &= L_1 z_1 + L_2 z_2 + L_3 z_3 \\ L_1 &+ L_2 + L_3 = 1 \end{aligned} \tag{A1}$$

and

$$\begin{aligned} x &= L_4 \tilde{x}_1 + L_5 \tilde{x}_2 \\ y &= L_4 \tilde{y}_1 + L_5 \tilde{y}_2 \\ z &= L_4 \tilde{z}_1 + L_5 \tilde{z}_2 \\ L_4 &+ L_5 = 1 \end{aligned} \tag{A2}$$

where $x_i, y_i, z_i,\ i = 1, 2, 3$—co-ordinates of three points in a plane, $\tilde{x}_1, \tilde{x}_2, \tilde{x}_3$ and $\tilde{y}_1, \tilde{y}_2, \tilde{y}_3$—co-ordinates of two points lying on the line. Then the L-co-ordinates of the point of intersection between the line and the plane are given by the solution of the following system of equations:

$$\begin{bmatrix} x_1 & x_2 & x_3 & -\tilde{x}_1 & -\tilde{x}_2 \\ y_1 & y_2 & y_3 & -\tilde{y}_1 & -\tilde{y}_2 \\ z_1 & z_2 & z_3 & -\tilde{z}_1 & -\tilde{z}_2 \\ 1 & 1 & 1 & 0 & 0 \\ 0 & 0 & 0 & 1 & 1 \end{bmatrix} \begin{Bmatrix} L_1 \\ L_2 \\ L_3 \\ L_4 \\ L_5 \end{Bmatrix} = \begin{Bmatrix} 0 \\ 0 \\ 0 \\ 1 \\ 1 \end{Bmatrix} \tag{A3}$$

The line intersects the plane inside the triangle when the conditions

$$L_i \in [0, 1], \quad i = 1, 2, 3 \tag{A4}$$

are satisfied.

REFERENCES

1. Soifer VA. Computer processing of images. *Herald of the Russian Academy of Sciences* 2001; **71**(2):119–129.
2. Zienkiewicz OC, Morgan K. *Finite Elements and Approximation*. Mir: Moscow, 1986; 320.
3. Bathe KJ. *Finite Element Procedures in Engineering Analysis*. Prentice-Hall: New Jersey, 1982; 735.
4. Ramesh K, Yadav AK, Pankhawalla VA. Plotting of fringe contours from finite element results. *Communications in Numerical Methods in Engineering* 1995; **11**:839–847.
5. Ramesh K, Pathak PM. Role of photoelasticity in evolving discretization schemes for FE analysis. *Experimental Techniques* 1999; **23**(4):36–38.
6. Vest CM. *Holographic Interferometry*. Wiley: New York, 1979.
7. Rastogi PK. Principles of holographic interferometry and speckle metrology. *Topics in Applied Physics* (*Photomechanics*) 2000; **77**:103–150.
8. Caponero MA, Pasqua P, Paolozzi A, Peroni I. Use of holographic interferometry and electronic speckle pattern interferometry for measurements of dynamic displacements. *Mechanical Systems and Signal Processing* 2000; **14**(1):49–62.
9. Vasiliauskas R, Palevicius A, Ragulskis K. Analysis of holographic interferograms by ultrasonic piezoelectric transducers in the investigation of three-dimensional vibrations. *Acoustical Physics* 1988; **34**(6):573–575.
10. Holstein D, Salbut L, Kujawinska M, Juptner W. Hybrid Experimental-numerical concept of residual stress analysis in laser weldments. *Experimental Mechanics* 2001; **41**(4):343–350.
11. Ivanov VP, Batrakov AS. *Three Dimensional Computer Graphics*. Radio i Sviaz: Moscow, 1995; 289.

